Experimental Investigation of Allotropic Transformation of Cobalt: Influence of Temperature Cycle, Mechanical Loading and Starting Microstructure

Nadjib Iskounen, Pierre-Antoine Dubos, Jamal Fajoui, Michel Coret, Marie-José Moya, Baptiste Girault, Nicolas Barrier, Nicolas Bruzy, Eric Hug, David Gloaguen

Experimental investigation of allotropic transformation of cobalt: influence of temperature cycle, mechanical loading and starting microstructure

Nadjib ISKOUNEN[a], Pierre-Antoine DUBOS[a*], Jamal FAJOUI[a], Michel CORET[a], Marie-José MOYA[a], Baptiste GIRAULT[a], Nicolas BARRIER[b], Nicolas BRUZY[a], Eric HUG[b], David GLOAGUEN[a]

[a] Université de Nantes - Centrale Nantes, Institut de Recherche en Génie Civil et Mécanique (UMR CNRS 6183), 58 rue Michel Ange - BP 420, 44606 Saint-Nazaire Cedex, France

[b] UNICAEN, Laboratoire de Cristallographie et Sciences des Matériaux (UMR CNRS 6508), 6 boulevard Maréchal Juin, 14050 Caen, France

[*]Corresponding author: pierre-antoine.dubos@univ-nantes.fr

Graphical abstract: Evolution of metastable cobalt FCC volume proportion during thermal cycle and mechanical loading.

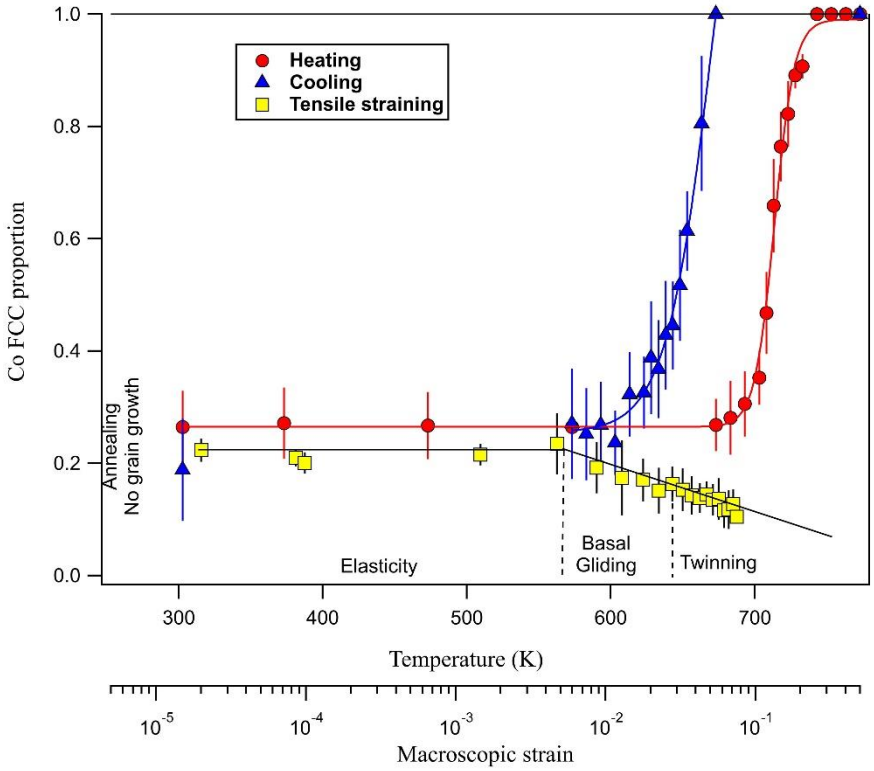

Abstract:

The allotropic phase transformation in polycrystalline high-purity cobalt is incompletely reversible and exhibits a temperature hysteresis. This leads to the presence of a FCC metastable phase at room temperature, which alters the mechanical properties. Moreover this phase transformation seems ~~to be able~~ to be induced by the plastic deformation. The influence of thermal cycling and initial microstructure on the phase transformation has been analyzed with different experimental approaches namely *in situ* X-ray diffraction, differential scanning calorimetry and high temperature digital image correlation analysis. A multiscale analysis, under an *in situ* tensile test, has been adopted to follow the phase transformation induced by the plastic deformation. The main result shows that the transformation is initiated by basal slip mechanisms, in competition with twinning mechanisms during the second work-hardening stage.

Keywords:

Cobalt, allotropic transformation, X-ray diffraction, plastic strain, crystallographic texture, *in situ* testing.

1. Introduction

Mechanical properties of metallic materials such as high-purity cobalt, are directly link to the crystallographic phase structures and microstructure defects presence. The mechanical behavior of two-phase cobalt remains unclear, when phase distribution and

evolution are not controlled. Results of the literature exhibited an important improvement of the mechanical properties of cobalt when it presents a two-phase structure [1].

High-purity polycrystalline cobalt exhibits an allotropic transformation (reversible and diffusionless) from HCP (Hexagonal Close-Packed) phase to FCC (Face Centered-Cubic) on around 713 K (austenitic transformation). The reverse transformation, from FCC to HCP phase (named martensitic transformation [2–4]), occurs roughly at 603 K. The cobalt transformations lead to a temperature hysteresis which depends on the number of applied thermal ~~transformation~~ cycles [4,5].

Most of the time, cobalt martensitic transformation remains incomplete. Consequently, a residual FCC phase persists at room temperature in association with the predominant HCP phase [3,6,7].

Sanderson [7] investigated the tensile properties of polycrystalline cobalt at room temperature so as to get the HCP phase stable, using different initial retained FCC phase volume proportions, grain sizes and purity samples. He found that the retained FCC phase volume fraction of polycrystalline cobalt, at room temperature, depends on the thermal history, the purity and the grain size. Marx *et al.* [8] studied by X-Ray Diffraction (XRD) the strain-induced phase transformation, at room temperature, in a 2 µm thick film deposited on polyimide substrate, using *in situ* tensile tests. They have shown that the untransformed metastable FCC phase was reduced from 51 % down to 8 % when the total macroscopic strain increases from 2 % up to 8 %.

Martinez *et al.* [9] investigated the dislocation microstructure of deformed polycrystalline cobalt by analyzing the different modes responsible for plastic strain. They have observed two distinct work hardening stages: a stage A, up to 4 % of plastic strain, where basal dislocation glide is the main deformation mechanism, and a stage B, where plastic

deformation is mostly accommodated by twinning mechanisms, in agreement with Seeger *et al.* [10]. These different deformation stages were also observed by Fleurier *et al.* [11]. HCP cold rolled metals tend to exhibit a specific deformation texture, called basal texture. A principal {00.1} basal texture component was indeed observed in polycrystalline rolled cobalt by Electron Back Scatter Diffraction (EBSD) [3,9]. The phase transformation in high-purity cobalt occurs by the glide of dislocations, due to the shear stress, on the habit $\{111\}_{FCC}//\{00.1\}_{HCP}$ planes [12]. Hesemann *et al.* [13,14] studied the influence of the texture on martensitic transformation in cobalt thin films, by varying the habit plane inclination angle from film surface, at different temperatures using *in situ* synchrotron XRD. They have observed that the phase transformation depends on the inclination angle between $\{111\}_{FCC}//\{00.1\}_{HCP}$ planes and the film surface, this transformation arising more easily at intermediary inclination of about 20°.

The present study focuses on the understanding of the allotropic transformation of polycrystalline high-purity cobalt, which might be affected by the initial microstructure as well as the thermal and mechanical loadings, using several characterization techniques. After a detailed description of the experimental methods, allotropic transformation behavior during thermal cycle, such as the evolution of the FCC phase volume proportion using *in situ* XRD laboratory technique, is presented. Moreover, the influence of the number of applied thermal cycles on the energetic parameters, carried out by Differential Scanning Calorimetry (DSC), is reported. On the other hand, an overview of the effect of the initial microstructure (modulated thanks to various annealing treatments) on the phase transformation is given. Finally, the strain effect on the phase transformation at room temperature is presented. *In situ* tensile tests under XRD have been used to study the influence of the strain hardening mechanisms onto the phase transformations.

2. Material and methods

2.1. Characterization of as-received material

Commercial polycrystalline cobalt sheets (Goodfellow Company) of high-purity (99.9 wt. %), cold-rolled to 0.5 mm in thickness, and with a recrystallized state, were used for the present study.

Metallographic examinations of the as-received material have revealed that the average grain size is about 24 µm, with a standard deviation of 12 µm. It appears that the initial microstructure displays two sets of grain shape corresponding to the two phases (HCP and FCC). **Fig. 1** shows a predominant polygonal grain family population, corresponding to the HCP phase, and a rather limited number of triangular and plate geometries for the FCC phase.

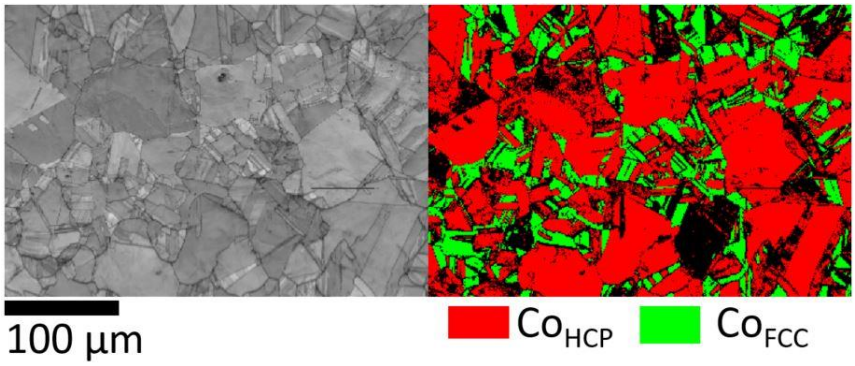

Figure 1: EBSD Image Quality (IQ) map and phase cartography of as-received cobalt microstructure.

Initial crystallographic textures and retained FCC phase ratio, at room temperature, were determined by XRD technique. A four-circle Seifert XRD3003 PTS diffractometer

equipped with an Euler cradle, a Position Sensitive Detector (PSD) with a 2θ effective windows of 8.6 °, a 1 mm diameter collimator and an IDS camera (in order to align the sample in the center of the goniometer), was used. A Cr anode ($CrK_{\alpha 1+2}$ radiation), operating at 30 kV and 35 mA, was used (wavelength λ = 2.28964 Å). The K_β component of the Cr radiation was eliminated using a vanadium filter installed in front of the detector.

Using θ - 2θ scanning mode, the diffraction spectra were recorded from 60° to 106° in 2θ with a step size of 0.05° and a counting time of 126 s/step. The analyzed reflections are listed in **Table 1**. The initial averaged FCC phase volume proportion, obtained according to the method described in the section 2.4.3, is about 22 %.

The crystallographic textures were determined from the Orientation Distribution Functions (ODF) calculated by the WIMV method implemented in the BEARTEX software [15], and were obtained from experimental Pole Figures (PFs) $\{10.0\}_{HCP}$, $\{00.2\}_{HCP}$, $\{10.1\}_{HCP}$,$\{10.2\}_{HCP,}$ $\{111\}_{FCC}$ and $\{200\}_{FCC}$ with average error coefficients in the order of 0.08, except for the initial FCC phase (0.2). The declination (ψ) and azimuthal (φ) angles varied from 0 to 65° ($\Delta\psi$ = 5°) and from 0 to 355° ($\Delta\varphi$ = 5°), respectively. At φ = 0° and ψ = 90°, the scattering vector was aligned with the Rolling Direction (RD).

2.2. Thermal cycles and Differential Scanning Calorimetry

The influence of the initial microstructure (grain size and retained FCC proportion) on the phase transformation was studied using DSC. First of all, cobalt samples were annealed at a temperature set between 573 K and 1273 K for 1 h, and cooled down with

a cooling rate of 40 K/min. In a second step, DSC scanning was performed on four samples (as-received and annealed at 573, 673 and 773 K) with a heating path up to 773 K then down to 593 K (heating and cooling rate = 10 K/min) according to the methodology described by Ray and Smith [2], in order to measure the HCP → FCC and FCC → HCP transformation temperatures. Ray and Smith [2] showed that the austenitic transformation temperature increases with higher heating rates. A phase quantification was carried out at 743 K with the same selected rate to ensure that the transformation was complete.

2.3. Macroscopic dilatometric test

Dilatometric tests have been performed using a homemade device on dog bone shaped tensile specimens [16,17]. The samples were machined by electroerosion along the rolling direction. The gage section is 5 mm ~~in~~ length, 5 mm ~~in~~ width and 0.5 mm ~~in~~ thickness. The sample is placed into a testing box under a low pressure of Argon and heated by Joule effect. A 2-color pyrometer (SensorTherm METIS M322) measures the temperature at the center of the specimen starting from 300° C, due to its intrinsic emissivity. Based on an alumina-based paint, a speckle pattern is deposited on the surface of the sample with a fine nozzle airbrush. During the test, a high-resolution camera (Prosilica GT6600 : 6576 × 4384 px^2) records images of a 9 × 6 mm^2 area. Macroscopic total strain field is then computed using Digital Image Correlation method (VIC software). The images and temperature values are recorded simultaneously, a establish the dilatometric curve (total strain versus temperature) ~~can finally be obtained~~.

2.4. *In situ* X-ray diffraction measurements

2.4.1. Temperature

In situ experiments have been carried out in order to study the influence of the temperature on the phase transformation behavior. The variation of phase (FCC and HCP) ratio during heating and cooling was evaluated by XRD technique on Bruker D8 advance diffractometer operating at 40 kV and 40 mA, equipped with a primary germanium (111) Johansson monochromator ($\lambda K_{\alpha 1}$ = 1.5406 Å) and a Lynxeye detector. The XRD patterns were recorded in the 2θ angular range 35 - 95° with a step size of 0.015° and a counting time of 0.9 s/step. The thermal cycle (with a rate of 0.5 K/s) was conducted between 303 and 773 K. Despite the short counting time, the signal-to-noise ratios are only slightly affected and the quality of the fitting shows, on average over all the peaks, an error of 0.0011° for the position and less than 5 % for the integrated intensities. The listed diffraction peaks presented in **Table 1** were monitored for each temperature of the thermal cycle described in **Table 2**. The temperature ranges and the heating step have been chosen around the temperatures of austenitic and martensitic transformations.

Table 1: XRD reflections tracked for each experiment and the plane family couples used for the phase volume fraction calculations.

	Studies		
	Strain influence on phase transformation	**Texture analysis**	**Thermal cycle influence on phase transformation**
HCP plane families	{10.0}, {00.2}, {10.1} and {10.2}		{10.0}, {00.2}, {10.1}, {10.3} and {10.2}
FCC plane families	{111} and {200}		
Planes family couples	$\{10.0\}_{HCP}/\{111\}_{FCC}$, $\{10.0\}_{HCP}/\{200\}_{FCC}$, $\{00.2\}_{HCP}/\{111\}_{FCC}$, $\{00.2\}_{HCP}/\{200\}_{FCC}$, $\{10.1\}_{HCP}/\{111\}_{FCC}$, $\{10.1\}_{HCP}/\{200\}_{FCC}$, $\{10.2\}_{HCP}/\{111\}_{FCC}$, $\{10.2\}_{HCP}/\{200\}_{FCC}$		$\{10.0\}_{HCP}/\{111\}_{FCC}$, $\{10.0\}_{HCP}/\{200\}_{FCC}$, $\{00.2\}_{HCP}/\{111\}_{FCC}$, $\{00.2\}_{HCP}/\{200\}_{FCC}$, $\{10.1\}_{HCP}/\{111\}_{FCC}$, $\{10.1\}_{HCP}/\{200\}_{FCC}$, $\{10.3\}_{HCP}/\{111\}_{FCC}$, $\{10.3\}_{HCP}/\{200\}_{FCC}$, $\{10.2\}_{HCP}/\{111\}_{FCC}$, $\{10.2\}_{HCP}/\{200\}_{FCC}$

Table 2: Applied temperatures for *in situ* XRD experiments during thermal cycle (heating rate 0.5 K/s between each temperature step – 1h acquisition duration for each temperature).

	Temperature range (K)	Temperature step (K)
Initial	At 303	-
Heating	From 373 to 673	100
	From 673 to 703	10
	From 703 to 733	5
	From 733 to 773	10
Cooling	From 773 to 673	100
	From 673 to 653	10
	From 653 to 623	5
	From 623 to 573	10
Final	At 303	-

2.4.2. Tensile tests

In situ uniaxial monotonic ~~uniaxial~~ tensile tests were carried out, at room temperature, to study the influence of elastoplastic strain on the allotropic transformation. These mechanical tests were performed on a DEBEN device, equipped with a load cell of 5 kN capacity, and controlled by the displacement between clamping jaws. The dog bone shaped tensile specimens were machined by electroerosion with a gage section of 26 mm ~~in~~ length, 7 mm ~~in~~ width and 0.5 mm ~~in~~ thickness ~~in three different directions with respect to RD: 0°/RD, 45°/RD and 90°/RD, latter corresponding thus to the Transverse Direction (TD)~~. In the same way, as explained in 2.3, the samples were also speckled and images were recorded during the test. Digital Image Correlation have then been processed to obtain the macroscopic total strain fields.

The samples were strained stepwise up to 7.8 % with a strain rate of 0.2 mm/min. At each straining step, and after a stress relaxation of about 20 minutes to obtain stable mechanical fields over the entire diffracting volume, the camera images were captured and the 2θ diffraction spectra were performed with an angle ranging from 60° to 106° with a step

size of 0.05° and a counting time of 126 s/step. The reflections listed in **Table 1** were analyzed. The crystallographic texture was also determined after the *in situ* tensile experiment as described in 2.1.

2.4.3. Analysis method

Experimental XRD peak profiles were fitted by a Pseudo-Voigt function which takes into account the $K_{\alpha1}$-$K_{\alpha2}$ doublet [18]. For each diffraction peak, background was fitted through a 2nd order polynomial function. Before peak profile analysis, angular corrections (Lorentz, polarization and absorption factors) are also applied [19].

The FCC phase volume fraction (denoted f^{FCC}) has been determined for each measurement point using the equation (1) as formulated by Bonarski *et al.* [20]:

$$f^{FCC} = \left(1 + \frac{I_{hkl}^{HCP}}{I_{hkl}^{FCC}} \frac{R_{hkl}^{FCC}}{R_{hkl}^{HCP}}\right)^{-1} \quad (1)$$

where I_{hkl} is the integrated intensity of the corresponding $\{hkl\}$ peak. R_{hkl} is the reflectivity of the lattice plane $\{hkl\}$, and is given by the following equation (2) introduced in the literature [20]:

$$R_{hkl} = \frac{1}{v^2} |F_{hkl}|^2 \left(\frac{1 + \cos^2(2\theta)}{\sin^2(2\theta)\cos(\theta)}\right) m \frac{e^{-2M}}{\mu} \quad (2)$$

where v is the volume of the unit cell (in Å^3), F_{hkl} is the structure factor, 2θ is the considered Bragg angle (in rad), m is the $\{hkl\}$ planes multiplicity factor, μ is the linear absorption coefficient (in cm^{-1}) and e^{-2M} is the Debye-Waller factor [21,22].

The volume fraction of the phases was calculated from several groups of family planes, as presented in **Table1**, to obtain the average FCC phase distribution and evaluate the influence of the texture on the quantitative phase analysis.

3. Results and discussion

3.1. Allotropic transformation characterization during thermal cycle

3.1.1. Phase proportion evolution and typical temperatures

In order to characterize the HCP ↔ FCC transformation behavior, the evolution of the integrated diffraction peak intensity for each reflection corresponding to the HCP and FCC phases were recorded as a function of the temperature. An example is given in **Fig. 2** for $\{111\}_{FCC}$ and $\{00.2\}_{HCP}$ reflections during heating and cooling. The volume fraction of the phases can be determined according to the equations (1) and (2).

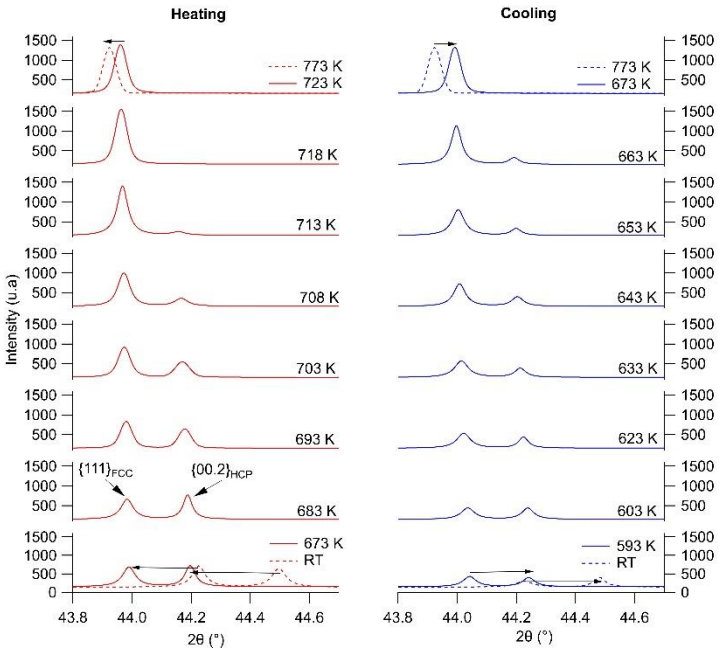

Figure 2: Diffraction patterns for $\{111\}_{FCC}$ and $\{00.2\}_{HCP}$ reflections during heating and cooling.

Fig. 3 gives FCC phase proportion evolution during the thermal cycle described in **Table 2**. During heating, the HCP → FCC transformation begins at the austenitic start temperature denoted A_s = 673 K and ends at the austenitic finish temperature named A_f = 743 K. During cooling, the reverse transformation FCC → HCP arises at the martensitic start temperature M_s = 673 K and comes back to its original state when the martensitic finish temperature of M_f = 593 K is reached. The two experimental curves can be fitted by sigmoidal laws which allow to define the transformation temperatures $T_{HCP\text{-}FCC}$ and $T_{FCC\text{-}HCP}$. These temperatures are determined when the FCC proportion has a relative variation of 50 % over the temperature cycle, knowing that the initial proportion is 26 % and that the transformation is complete during heating. With this methodology, $T_{HCP\text{-}FCC}$ = 714 K and $T_{FCC\text{-}HCP}$ = 653 K are obtained, revealing a temperature hysteresis around 60 K. One can notice that the diffraction patterns have also enabled to identify CoO and Co_3O_4 oxides formation from 673 K that persist when cooling down to room temperature. It is important to point out that the presence of a thin oxide layer does not affect the quantification of the HCP and FCC phase proportions. Finally, it seems that the phase transformation is faster during heating than during cooling. This can be related to the phase transformation mechanism which is based on dislocation movements [23], themselves favored by an increase in temperature.

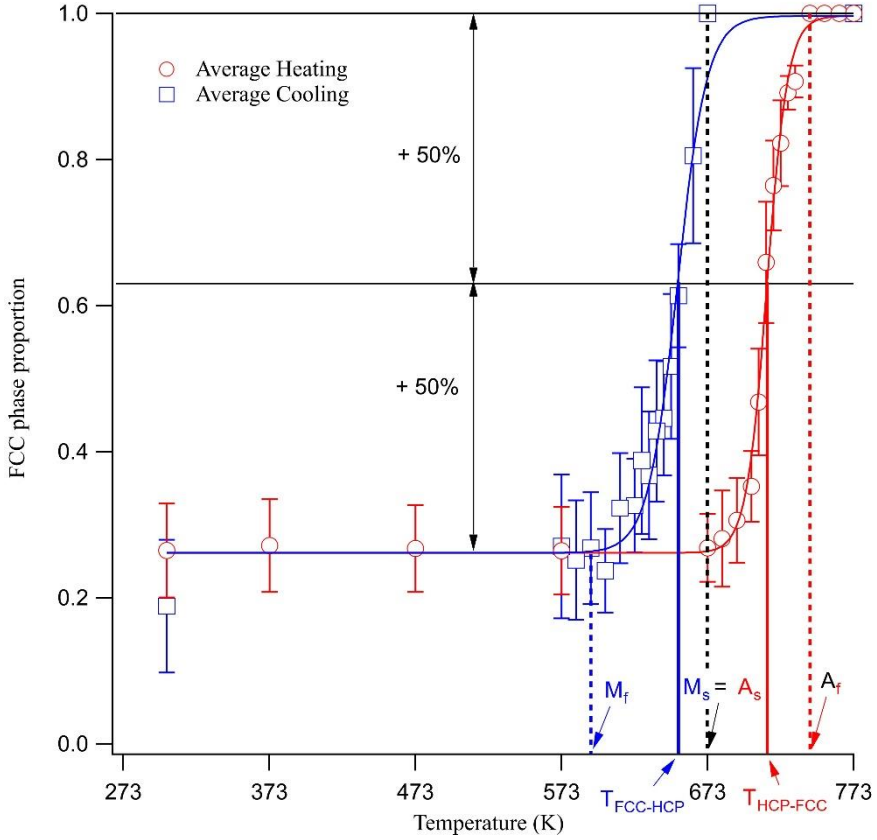

Figure 3: Volume fraction of FCC phase during heating (red circle) and cooling (blue square) of cobalt calculated from XRD data. Error bars are the standard deviation on the 8 couples of family planes.

3.1.2. Lattice strain measurements during the thermal cycle

Lattice strain of each {hkl} plane family can be determined considering lattice spacing (d_{hkl}) as an elastic strain gage using the following equation [24]:

$$\langle \varepsilon(hkl) \rangle_{V_d} = \ln\left(\frac{\langle d^{hkl} \rangle_{V_d}}{d_0^{hkl}}\right) = \ln\left(\frac{\sin\theta_0(hkl)}{\langle \sin\theta(hkl) \rangle_{V_d}}\right) \quad (3)$$

$\langle \varepsilon(hkl) \rangle_{V_d}$ is the elastic lattice strain. $\langle\ \rangle_{V_d}$ indicates an averaging over diffracting grains for the considered {hkl} reflection. For a given {hkl} reflection, d_0^{hkl} and $\theta_0(hkl)$ are the interplanar spacing and the diffraction angle (Bragg angle), respectively, in the

undeformed sample i.e. prior to any thermal or mechanical loading. **Fig. 4(a)** gives the evolution of the lattice strains observed for different {hkl} reflection of the two phases during the applied thermal cycle. This evolution is linear for both heating and cooling, enabling to estimate the Coefficients of Thermal Expansion (CTE) α_{hkl} for each plane family within the analyzed polycrystal. The obtained values are represented in **Fig. 4(b)** and are in agreement with the literature [21]. Matsumoto [4] has also shown that the CTE of HCP single crystal is substantially affected by the orientation of the *c*-axis within the sample coordinate system. Thermal cycle induces a large strain, the largest one actually reaches more than 8000 µ-strain ($\times 10^{-6}$ mm/mm) for the $\{00.2\}_{HCP}$ set of grains. The main thermal dilatation occurs then along the $[00.2]_{HCP}$ direction. During cooling, plastic deformations are induced and can be explained by the presence of residual lattice strains. These results agree with prior investigations on high-purity cobalt showing slipping lines due to plastic deformation during the thermal cycle [23,25].

Fig. 4(c) shows the residual lattice strains present after the thermal cycle for each analyzed reflection. Initially, residual strains can be considered negligible due to the annealed character of the as-received materials. This allows considering the initial state of samples as a strain-free reference. After the thermal cycle, residual lattice strains have slightly increased, especially for $\{00.2\}_{HCP}$, $\{10.2\}_{HCP}$ and $\{200\}_{FCC}$ reflections. Regarding uncertainties, only $\{00.2\}_{HCP}$ planes present an unambiguous residual strain of a few hundred of µ-strains in tension. As shown in **Fig. 4**, these residual strains measured after a thermal cycle are related to the phase transformation and its associated volume variation as well as the accommodation related to the thermal and plastic anisotropies.

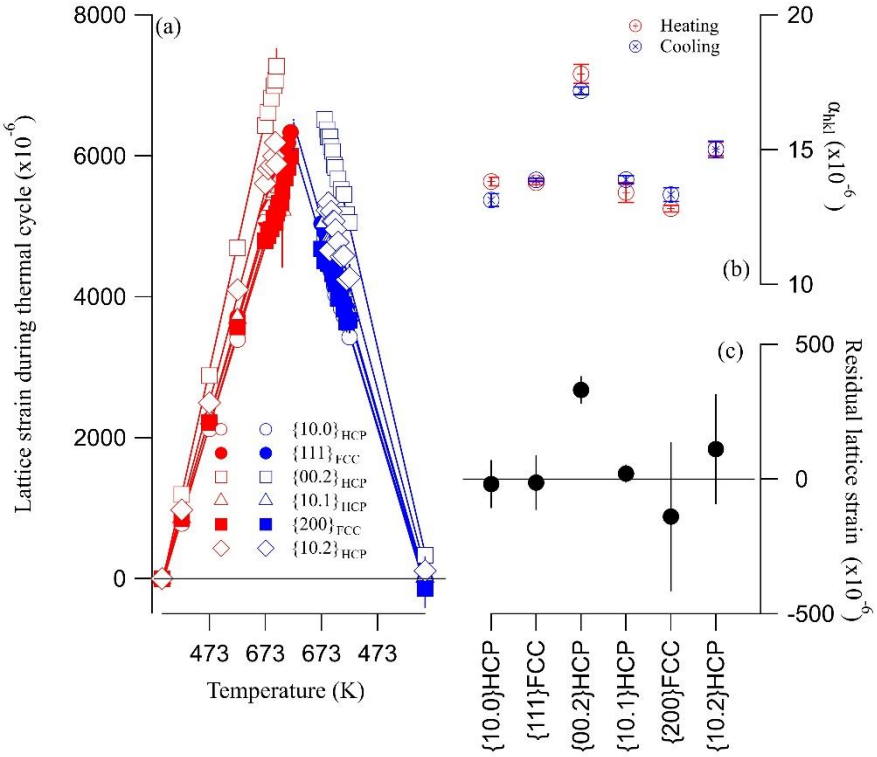

Figure 4: Mechanical state during thermal cycle considering the different tracked plane families. (a) Lattice strain evolution during heating (red) and cooling (blue). (b) Thermal expansion coefficients during heating (red open circle) and cooling (blue open circle) obtained from XRD results. (c) Measured residual lattice strains after (black solid circle) the thermal cycle.

3.1.3. Macroscopic thermal dilatation

The post-treatment of image correlation results enables to access to ε_{xx} (parallel to RD), ε_{yy} (parallel to the transverse direction (TD)) and γ_{xy} strain components. **Fig. 5** shows the dilatometric curves obtained by coupling the temperatures measured by pyrometer (at the center of the sample) and the strain fields obtained by image correlation method. The phase transformation induces a change of volume, due to the change of the lattice structures, of about 0.3 % in the case of high-purity polycrystalline cobalt, as reported in the literature [12,25,26]. Hence, in the temperature range between 573 K and 773 K, the

289 dilatometric curve is the consequence of the competition between thermal expansion and
290 volumetric change. As it can be seen, both dilatometric curves along x and y display a
291 temperature hysteresis caused by the phase transformation, which is not observed on the
292 lattice strains during the thermal cycle (see **Fig. 4(a)**). The difference in the scale of
293 analysis may be the reason for these observations. XRD results exhibit the combination
294 of macroscopic (or Type-I) and intergranular strains (or Type-II) whereas dilatometry
295 only gives access to macroscopic strains. The hysteresis of ε_{xx} dilatometric curve is
296 qualitatively slightly broader than the one of ε_{yy} dilatometric curve and could be explained
297 by a slight anisotropy or texture effect. Moreover, hysteresis occurs systematically
298 between the temperatures $M_f = 593$ K and $A_f = 743$ K. Beyond austenitic finish
299 temperature, A_f, the dilatometric curve displays a linear evolution (for both of ε_{xx} and ε_{yy})
300 with temperature that matches a pure thermal expansion or contraction during heating or
301 cooling, respectively. ε_{xx} and ε_{yy} strain components exhibit a quasi equibiaxial strain state
302 with an order of magnitude similar to the measured lattice strains induced by the thermal
303 cycle (see **Fig. 4**). Finally, the dilatometric curve of γ_{xy} clearly highlights the absence of
304 macroscopic planar shearing during the thermal cycle.

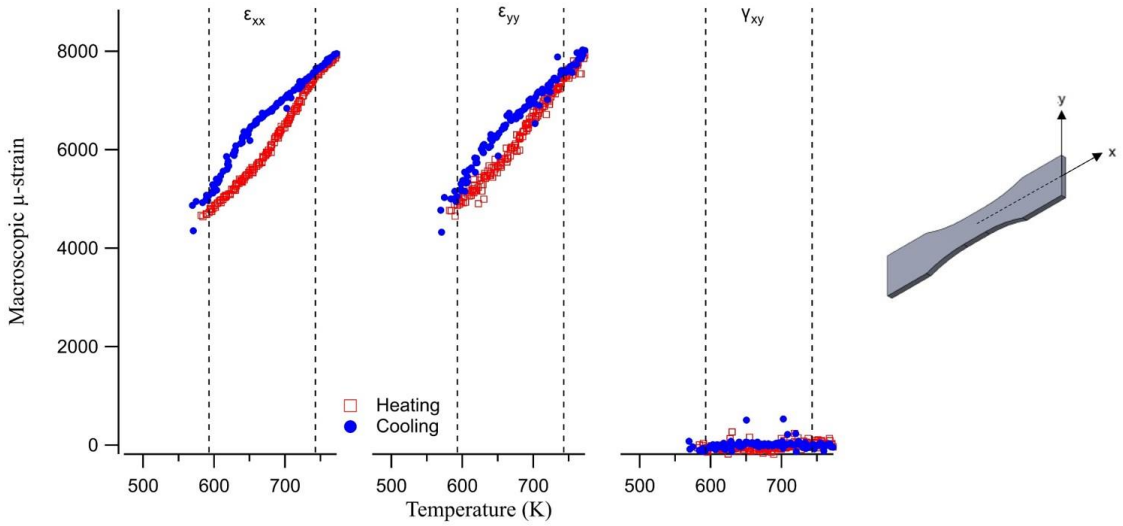

305

306 **Figure 5:** Dilatometric curves according to ε_{xx}, ε_{yy} and γ_{xy} during the thermal cycle. (x
307 corresponds for this experiment to the rolling direction).

308

309 *3.1.4. Influence of initial microstructure on the allotropic transformation*

310 **Fig. 6** shows the influence of annealing temperature on the grain size and on the volume
311 fraction of the retained FCC phase. In the present work, an annealing duration of one hour
312 has been chosen in order to have a limited granular growth so that grain size evolution
313 remains a minor contribution to the microstructure changes no matter the selected
314 annealing temperature. These results are then compared with previous works for a 1373 K
315 annealing temperature with durations ranging from 1 to 96 hours [27]. The grain size,
316 deduced from metallographic observations, slightly increases with annealing temperature
317 but does not seem very significant as compared to the power type increase appearing from
318 20 hours of heat treatment at 1373 K. Concerning the proportion of retained FCC phase,
319 it exponentially decreases from 28 % (as-received) down to almost 10 % for 873 K
320 annealing, in accordance with Sanderson [7]. For annealing temperatures greater than
321 873 K or longer annealing durations, this proportion remains constant.

Overall, these results allow to explain the final FCC phase proportion met after the thermal cycle. In fact, the thermal cycle applied during the previous *in situ* analysis was including a heating stage until 773 K. This treatment has induced a complete transformation of the HCP phase and significantly reduced the proportion of residual FCC phase at room temperature.

The results of **Fig. 6** clearly show that annealing treatments at moderate temperature ($T_{annealing} < T_{HCP\text{-}FCC}$) enable to homogenize the microstructure with a reduction of the retained FCC proportion combined with a limited grain growth. The energy required for phase transformation is much lower than the one for grain growth, showing to some extent the independence of these two phenomena.

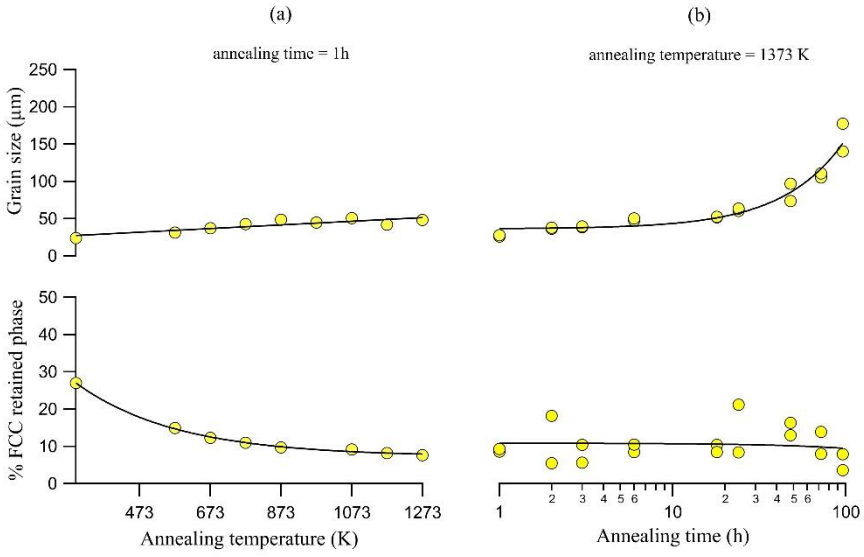

Figure 6: Influence of annealing conditions (temperature for a time of 1h (a) and time for a temperature of 1373°K (b)) on grain size and retained FCC phase proportion evolution.

The influence of initial microstructure (i.e. retained FCC phase ratio and grain size to a lesser extent) on the phase transformation, performed using DSC, is plotted in **Fig. 7**. Austenitic and martensitic transformation peaks are tracked during the DSC thermal cycle, on the as-received Co specimen as well as on the 573 K, 673 K and 773 K annealed samples with 40 K/min cooling rate. The temperature of the HCP → FCC transformation increases with annealing temperature. The results show that the temperature to initially transform the HCP phase is directly related to the initial proportion of the retained FCC phase: the higher the annealing temperature, the lower the retained FCC volume fraction and the higher the HCP → FCC phase transformation temperature. Indeed, austenitic transformation needs more thermal energy to enable phase transformation as HCP volume fraction to be transformed increases. In return, since the reverse transformation (i.e., FCC → HCP) takes place during cooling with 100 % FCC phase (austenitic transformation is completely finished at 773 K), the martensitic transformation temperature is then unchanged during cooling.

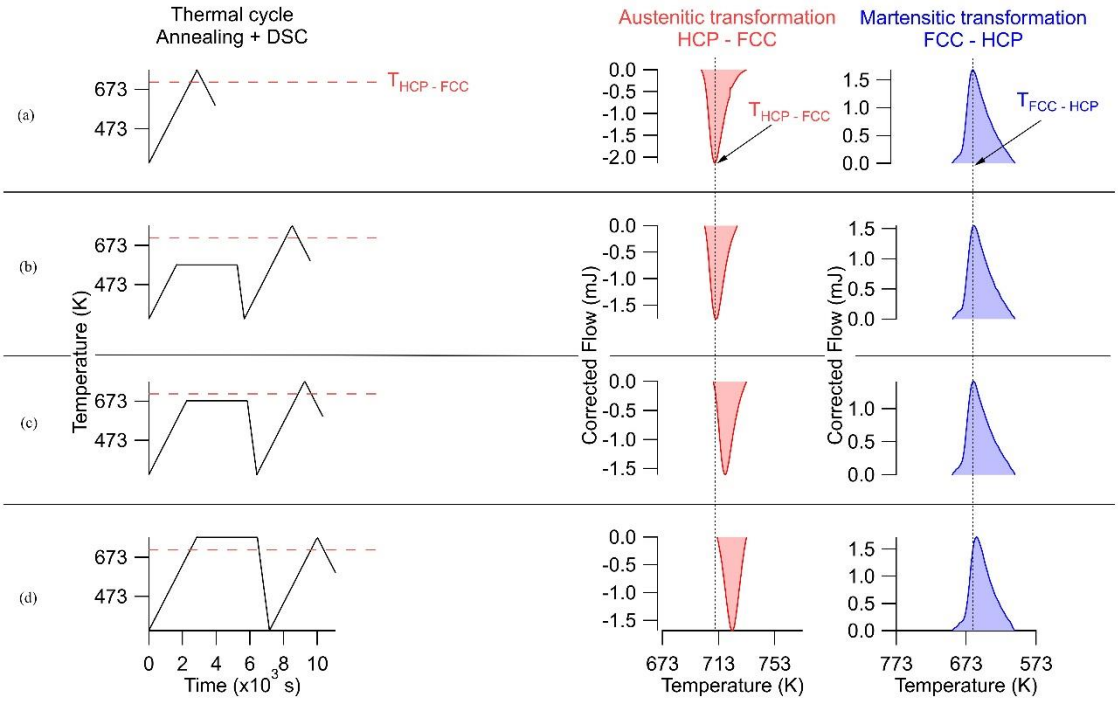

Figure 7: Thermal loading paths in DSC performed for as-received (a), 573 K (b), 673 K (c) and 773 K (d) annealed samples with corresponding austenitic (red) and martensitic (blue) transformation peak tracking.

Despite a microstructure that appears to be stable, when subjected to thermal cycles around the transformation hysteresis (593 K – 773 K), the sample annealed at 773 K during one hour shows (see **Fig. 8**) an austenitic temperature which only becomes stable after about 15 cycles. It could be noted that the austenitization temperatures of the as-received sample and the two other annealed samples stabilize at the same value (≈ 721 K). This observation shows that it is necessary to transform the material about fifteen times in order to homogenize it and to make its temperature $T_{HCP\text{-}FCC}$ independent of the following heat treatments. As displayed in **Fig. 8**, the martensitic transformation temperature does not depend on the initial microstructure and therefore on annealing temperature. This is convenient with the fact that it transforms the same FCC phase proportion (*i.e.* 100 %). In the same way, this transformation is insensitive to the number of thermal cycles as the $T_{FCC\text{-}HCP}$ temperature varies less than 2 K.

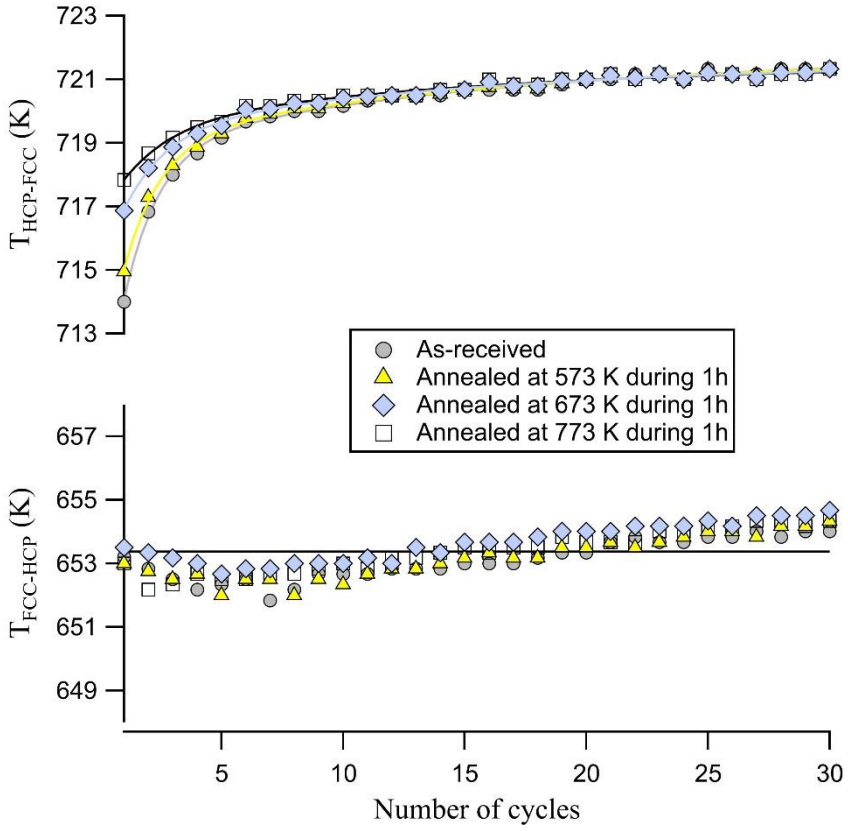

Figure 8: Temperatures of HCP → FCC and FCC → HCP transformations as a function of the number of applied DSC cycles (up to 30 cycles) of as-received sample superposed with the result of 573 K, 673 K and 773 K annealed samples.

Bauer et *al.* [23] showed a grain growth of 15 to 80 µm with 60 DSC cycles, which does not influence the stabilized transformation temperature after 15 cycles. An additional study was carried out on samples with different grain sizes and the same FCC proportion (d = 100 µm, f_{FCC} = 0.1 for an annealed sample during 48 hours at 1373 K and d = 25 µm f_{FCC} = 0.1 for an annealed sample during 1 hour at 1373 K). The stabilized transformation temperature after 30 cycles is clearly independent of the initial grain size.

3.2. Allotropic transformation during mechanical deformation

3.2.1. Phase proportion evolution and work-hardening during tensile test

The mechanical behavior in tension can be divided in three distinct stages. The first one is the elastic part. Zhou *et al.* [28,29] have shown that this stage is characterized by a kinking nonlinear elasticity resulting in fully reversible hysteresis induced by nucleated dislocation loops in the slipping favored plane (the basal plane in the present case).

The second one, named stage A, characterizes the first work-hardening stage and appears from a strain of 0.0045 up to 0.018 (**Fig. 9**). This stage is associated with a large reduction of the work-hardening rate and is controlled by planar and single glide of basal dislocations [9]. However the combination of basal slip and volume change during transformation [26] does not satisfy von Mises criterion which requires, for a polycrystal, five independent shear systems to undergo homogeneous strain without changes in volume. In order to accommodate the plastic deformation and since the FCC to HCP phase transformation is a low energy transformation requiring only simple shear, the formation of martensitic phase can be considered as equivalent to the formation of twins.

Above a strain level of 0.018, the slope of the work-hardening rate is lowered to an almost constant value corresponding to stage B. This stage is described by twinning nucleation and growth. Martinez *et al.* have shown that compression $\{10.1\}_{HCP}$ and tensile $\{10.2\}_{HCP}$ twins are the main twinning modes representing respectively 16 % and 66 % of total observed twin planes [9].

Fig. 9 highlights the effect of these deformation mechanisms on the allotropic transformation, for tensile sample strained along the rolling direction. The fast track FCC phase proportion, determined from θ - 2θ spectra achieved at ($\psi = 0$ °, $\varphi = 0$ °), is plotted (open triangles) versus the macroscopic applied true strain. This figure shows a transformation of the initial residual FCC phase into HCP phase initiated by plasticity.

From the beginning of stage A to the end of stage B, this transformation is done gradually and linearly with the logarithm of the applied strain. In order to ensure reliability and reproducibility of the experimental data, the tests were repeated three times by three different investigators. The FCC phase proportion evolution during tensile loading can be expressed by the following proposed straightforward equation:

$$\text{FCC proportion} = a * \log(\varepsilon) + b, \quad (4)$$

where coefficients are a = -0.089 ± 0.006, and b = 0.017 ± 0.01, with a linear regression coefficient R^2 = 0.93. In comparison, Sanderson found a = -0.1 and b = 0.019 for polycrystalline samples with 10 µm grain size [6]. The experimental slope is similar in stage A and in stage B, leading to the conclusion that the phase transformation does not seem to be affected by the activation of twinning during stage B.

In order to take into account a doubtless evolution of the texture with the mechanical loading and to study the anisotropy of the phase transformation, FCC phase proportion is determined for each of the (ψ, φ) couples covering a quarter of a pole figure (0 ° < ψ < 55 °, 0 ° < φ < 90 °) using the 8 plane family couples detailed in **Table 1**. Values are then averaged and results are plotted (red solid circles named ¼ PF) in **Fig 9**. Phase ratio evolution shows the same tendency as the one determined at (ψ = 0 °, φ = 0 °) for the two plasticity stages, with the same slope but a *b*- coefficient equal to 0.117±0.007. However, these averaged values are higher due to the influence of the texture on the phase proportion quantitative determination. Calculations of the phase proportion taking into account the ODF (red open lozenges in **Fig. 9**) from complete recalculated PFs have been performed on the as-received material and on a specimen strained at 0.078 in order to confirm the relevance of the results obtained over a quarter of experimental PF under

loading. As regard to the experimental complexity to carry out ODF and since the texture does not fundamentally change the results, the choice is made to simplify the quantification of phase proportions at a single position (i.e. $\psi = 0°$, $\varphi = 0°$).

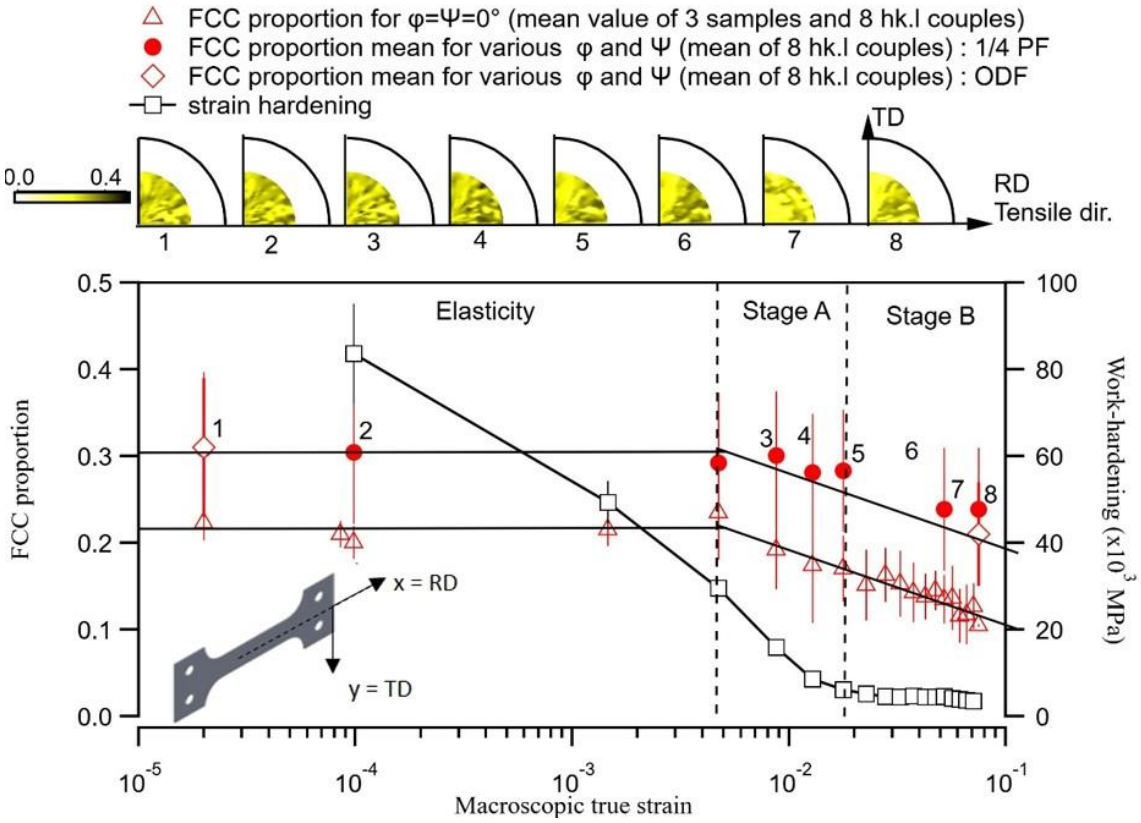

Figure 9: FCC → HCP transformation evolution as macroscopic strain increases. Relationship between FCC phase proportion (red open triangle) and the deformation stages illustrated by work-hardening (black open square). Monitoring of the phase transformation anisotropy for various (φ, ψ) orientations (maps) during tensile straining with the corresponding average values (red solid circle).

3.2.2. Crystallographic analysis of the strain-induced phase transformation and the deformation mechanisms.

Deformation mechanisms and phase transformations can be explained by a crystallographic analysis, comparing the different texture components observed on the

recalculated PFs obtained thanks to XRD on a sample before and after straining. **Fig. 10** shows $\{10.0\}_{HCP}$, $\{00.2\}_{HCP}$, $\{10.1\}_{HCP}$, $\{10.2\}_{HCP}$, $\{111\}_{FCC}$ and $\{200\}_{FCC}$ recalculated PFs of the as-received sample and of a sample strained at 7.8 % along RD. Except for the habit plane between HCP and the retained FCC, it can be assumed that the initial state of the HCP phase is not textured as compared to the deformed state that exhibits distinctive poles which can be seen on the majority of PFs [30].

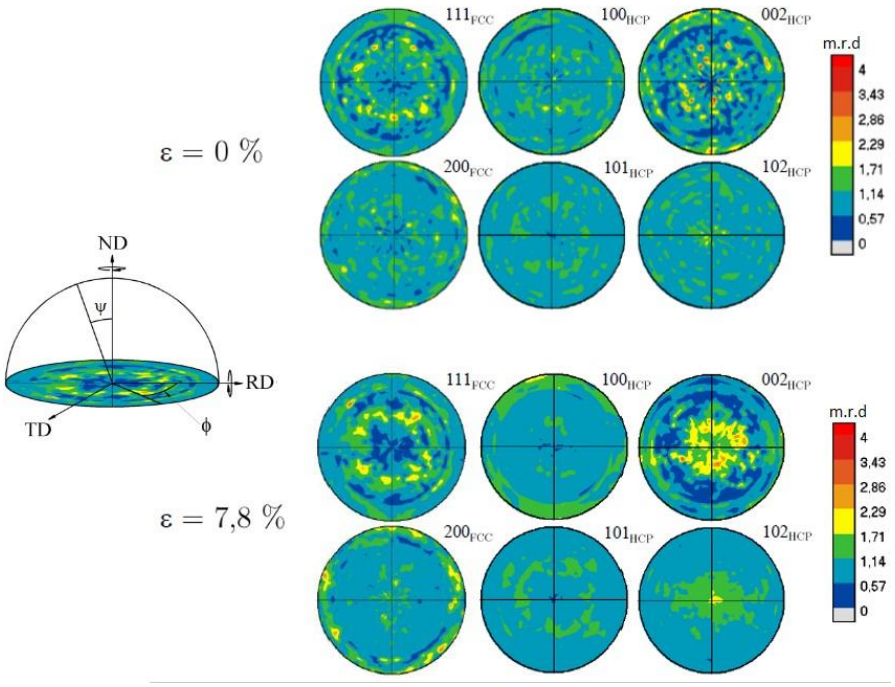

Figure 10: $\{10.0\}_{HCP}$, $\{00.2\}_{HCP}$, $\{10.1\}_{HCP}$, $\{10.2\}_{HCP}$, $\{111\}_{FCC}$ and $\{200\}_{FCC}$ recalculated PFs of the as-received sample and of a sample strained at 7.8 % along RD.

If the sample shows an isotropic orientation distribution in the initial state, three specific orientation cases of the HCP lattice with respect to the loading direction are assumed to be sufficient to study the orientation dependence of deformation mechanisms and phase transformation: *c-axis* parallel, normal or inclined with respect to the loading direction, as shown in **Table 3**.

Table 3: {00.2} and {10.0} PF reorientations peculiar to twinning systems and phase transformation according to the 3 studied configurations.

	Twinning system [31]	**Twinning shear** [32–34]	**ψ-angle reorientation on {00.2} PF**	**ψ-angle reorientation on {10.0} PF**
(a) Tension twin **σ//*c-axis***	{10.2} < 10.1 >	0.13	5°	85°
(b) Compression twin **σ⊥*c-axis***	{10.1} < 10.2 >	0.14	56°	34°
(c) FCC-HCP transformation **σ//(10.2)**			43° (111) 66° ($11\bar{1}$)	

As described in the 3.2.1 subsection, the plastic behavior of high-purity polycrystalline cobalt exhibits two distinctive stages which correspond to the activity of basal slip (stage A) and twinning deformation modes (stage B). The determination of Schmid's factor of the basal plane for the three specific orientation cases (σ//*c-axis* (a), σ⊥*c-axis* (b) and σ//(10.2) (c)) shows that the unique configuration enabling such a slipping activity is (c): (10.2) plane parallel to the specimen surface with a Schmid's factor close to 0.5 (most suitable configuration for basal slip). Configurations (a) and (b) will then be the most likely to show twin activity. Two types of twins have been frequently observed in deformed high-purity polycrystalline cobalt [9,33]. The first one is the tensile twin {10.2}<10.1>, which activates when the HCP lattice undergoes a tensile strain along the *c-axis*, because of the ratio $c/a < \sqrt{3}$ [32]. It represents 66% of the observed twinning modes in deformed cobalt and leads to a crystal rotation of 85°. The second one is the

compression twin {10.1}<10.2>, observed at a level of 16% and associated with a crystal rotation of 56°.

In addition to the deformation mechanisms, strained cobalt also presents ~~also~~ a phase transformation FCC → HCP, which is diffusionless and occurs by dislocation gliding on the habit plane {111}//{00.2}, causing shear along the $[11\bar{2}]_{FCC}$ direction (equivalent to the HCP direction [11.0]). The phase transformation is called multi-variant due to its capability to occur on several $\{111\}_{FCC}$ planes, which display rotation angles of 70.53° between them [12] (illustrated in **Fig. 11**). However, due to the compactness difference between the two phases, the resulting rotational angle after the phase transformation FCC → HCP becomes 71.4° according to the orientation relationship established by Shoji-Nishiyama [35]. Hence, the resulting crystal undergoes a theoretical volume change of about -0.3 %, which corresponds to a slight contraction along the *c-axis* [26,36]. This phase transformation is more likely to be initiated when the habit plane {111}//{00.2} shows an intermediary inclination as regard to the loading direction [13,14] corresponding to (c) configuration in **Table 3**. The crystallographic mechanism of FCC → HCP phase transformation is illustrated in **Fig. 11**, showing the FCC lattice atoms displacement along the $[11\bar{2}]$ direction and the formation of the HCP lattice from three {111} FCC planes.

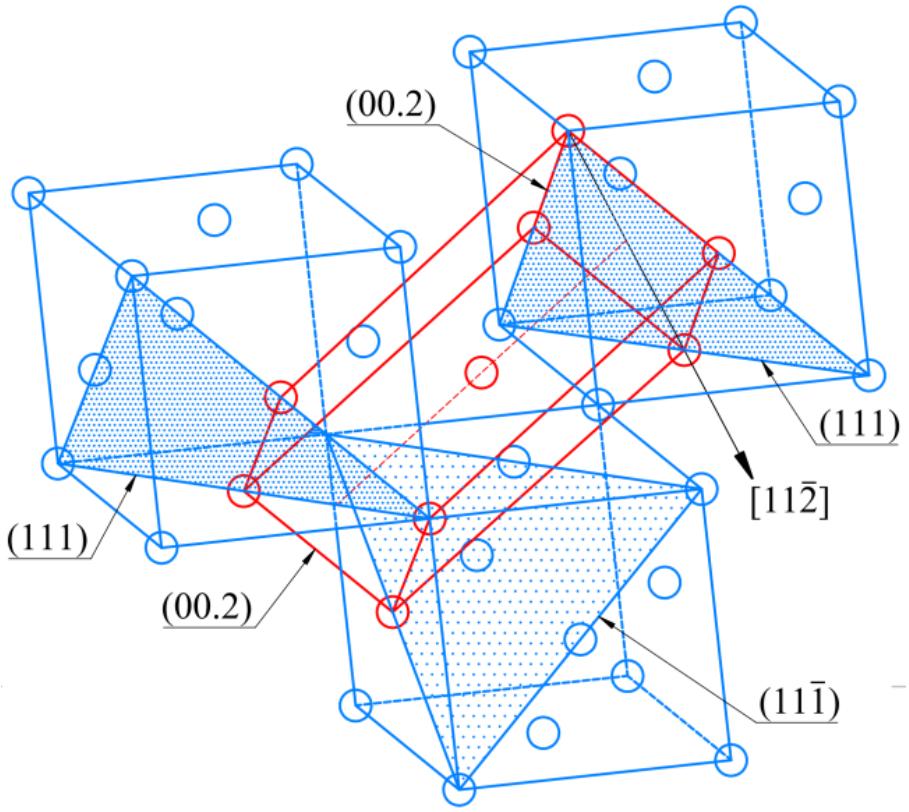

Figure 11: Schematic representation of the orientation relationship between the FCC structure (in blue) and the HCP structure (in red) once shear has been achieved along the [11$\bar{2}$] FCC direction.

The crystallographic analysis carried out on the PFs of the deformed sample highlights the activated twin modes as well as the FCC → HCP phase transformation induced by mechanical loading. It should be underlined that only two twin systems ({10.2}<10.1> for configuration (a) and {10.1}<10.2> for configuration (b)) have been clearly identified using the PFs of the sample loaded up to 7.8 % strain. Those actually match the lowest shear twinning values [32–34].

In the first configuration considered (a), the tensile twin mode {10.2}<10.1> induces a crystal reorientation of 85°. This configuration concerns the reorientation of 85° of the *c-axis*, which were initially parallel to the loading direction (displayed by the orange solid

line lattice projection in **Fig. 12 b**) and become misaligned by 5° as compared to the normal of the sheet plane (ND) (displayed by orange dashed line lattice projection in **Fig. 12 b**). For the twinned part, it results in an angle of 85° between ND and the normal of the twinned prismatic plane (10.0) and an angle of 5° between ND and the normal of the twinned basal plane (00.2). These crystallographic reorientations of the twinned region as compared to the parent crystal is depicted by intensity reinforcement arcs on {00.2} and {10.0} PFs at 5° and 85° (identified by dashed orange rings in **Fig. 12 a**), respectively. On the {10.0} PF, the orientation reinforcement is preferably done at 90° from the loading direction in the sheet plane (TD).

In the second configuration considered (b), the compression twin mode {10.1}<10.2> causes a crystal reorientation of 56°. Therefore, the resulting orientations of the twinned basal plane (00.2) and twinned prismatic plane (10.0) to the sample surface are 56° and 34°, respectively (displayed by pink dashed line lattice projection in **Fig. 12 b**). These crystallographic reorientations are highlighted by intensity reinforcement rings (dashed pink rings in **Fig. 12 a**) that can be observed on {00.2} and {10.0} PFs at 56° and 34°, respectively.

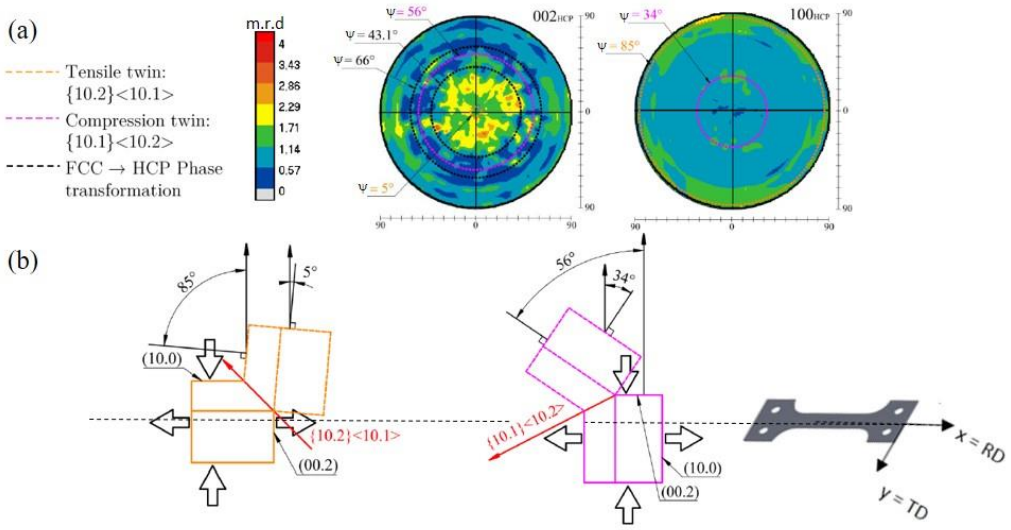

519

520 **Figure 12:** Identification of {10.2}<10.1> tensile twinning system, {10.1}<10.2>
521 compression twinning system and phase transformation on {00.2} and {10.0} PFs for the
522 sample loaded up to 7.8 % strain (a). Schematic representation of reorientations caused
523 by the two twin systems (b).

524

525 In the third configuration considered (c): the FCC → HCP phase transformation induced
526 by tensile straining can be observed on {10.2}, {00.2}, {111} and {200} PFs (dashed
527 black circle in **Fig. 12 a** and **Fig. 13 a**). Because of the intermediate inclination of the
528 HCP lattice, the (10.2) HCP plane is parallel to the sheet plane. Thus, the ND matches the
529 central pole (at $\psi = 0°$) observed on the {10.2} PF. As described above, the FCC → HCP
530 phase transformation is multi-variant, and may occur on several {111} FCC planes. For
531 this configuration and considering the Shoji-Nishiyama's relationship, the habit plane
532 (111)//(00.2) is at an angle of 43.1° to the sample surface and the $(11\bar{1})$ one at an angle
533 of 66°, as illustrated on $\{00.2\}_{HCP}$ and $\{111\}_{FCC}$ PFs (dashed black circle in **Fig. 12 a** and
534 **Fig. 13 a**). Finally, the (200) FCC plane is oriented at 79° to the ND and depicted by an
535 intensity reinforcement located at this ψ value on the $\{200\}_{FCC}$ PF.

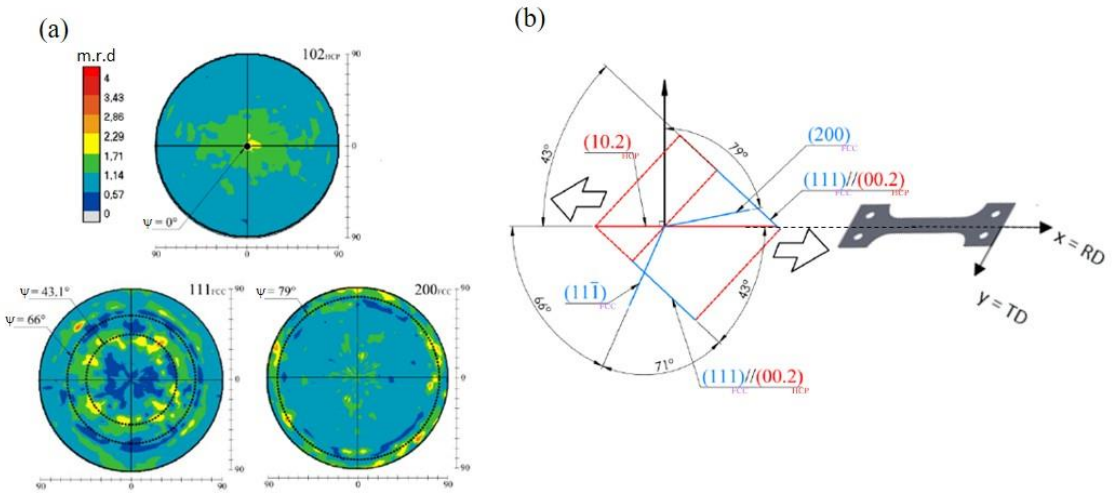

536

537 **Figure 13:** Identification of the phase transformation from $\{10.2\}_{HCP}$, $\{111\}_{FCC}$ and
538 $\{200\}_{FCC}$ PFs for the sample loaded up to 7.8 % (a). Schematic representation of
539 misorientations caused by the phase transformation (b).

540

541 Another way to analyze the evolution of the FCC → HCP phase transformation with the
542 mechanical loading as well as the evolution of the main tensile twin deformation mode
543 ({10.2}<10.1>) is to follow the integrated intensities of the peaks reflecting these two
544 phenomena. **Fig. 14** shows the tracking of the integrated intensities of {00.2} and {10.2}
545 peaks during straining (for ψ respectively close to 5° and 0°) which correspond,
546 respectively, to the activity of the twinning mode {10.2}<10.1> and the FCC → HCP
547 phase transformation. It can be seen that the integrated intensity of the peak {00.2}
548 remains unchanged during straining until the beginning of stage B for which plasticity is
549 governed by twinning. Thereafter, the integrated intensity of the {00.2} reflection linearly
550 increases with the macroscopic strain. The monitoring of the integrated intensity of the
551 {10.2} peak shows that the phase transformation, initiated by basal slip, starts at the
552 beginning of the plasticity, in agreement to the results obtained for the FCC volume
553 fraction evolution (see **Fig. 9**). Subsequently, the integrated intensity of the {10.2} peak
554 increases with macroscopic strain until the end of stage A. At this strain level, the

555 twinning mechanism is activated and becomes the main deformation mode, which causes
556 a lattice reorientation and a possible stress relaxation. Therefore, the slope of the
557 integrated intensity evolution of {10.2} reflection tends towards 0, and remains
558 unchanged with increasing macroscopic strain. Thus, at stage B, the evolution of the
559 integrated intensity of the {10.2} reflection seems to reflect a competition between the
560 phase transformation and the twinning process.

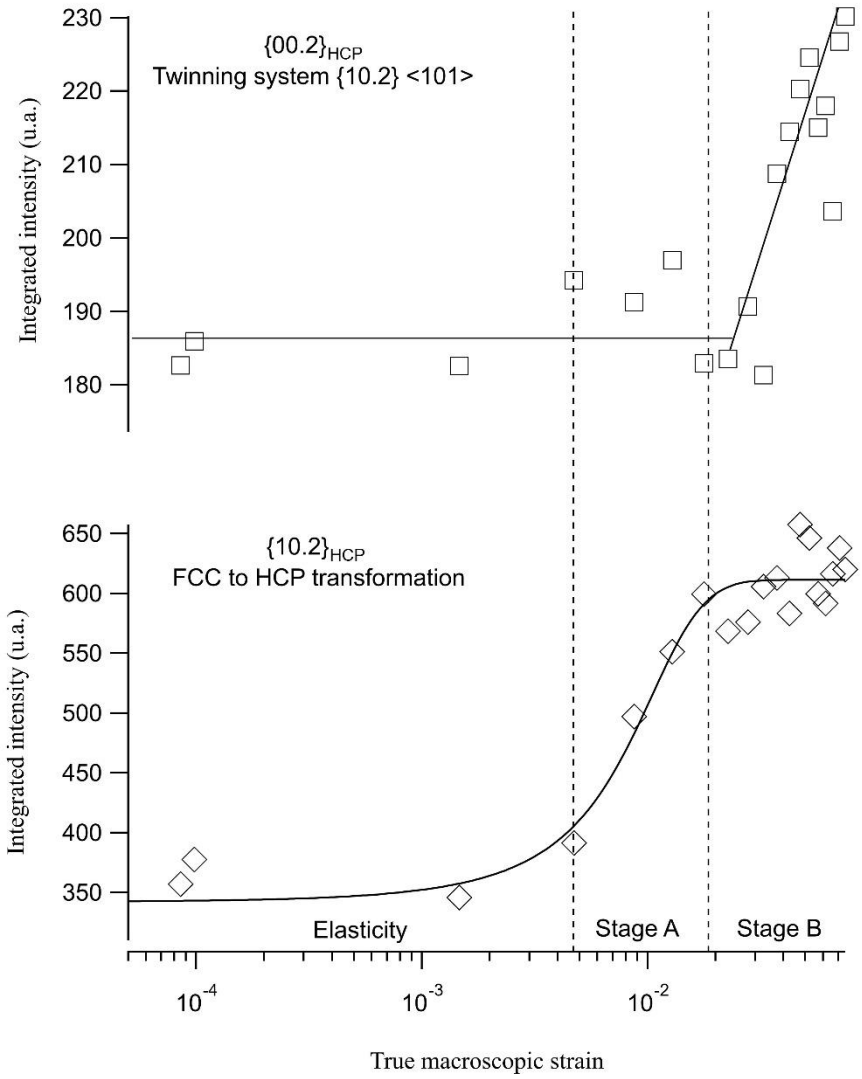

561

562 **Figure 14:** Evolution of the integrated peak intensity at ψ = 0° for the {10.2} reflection
563 and around ψ = 5° for the {00.2} reflection during a tensile test along the rolling direction.

564

The monitoring of internal lattice strains (determined using the eq. (3)) of some {hkl} plane families of HCP and FCC phases during tensile tests is illustrated on **Fig. 15**. In order to compare these results with those obtained during the cooling of the thermal cycle (subsection 3.1.2), the internal lattice strains related to the two loading types (thermal and mechanical) are thus superimposed while adapting the temperature range of the thermal loading to the FCC → HCP phase transformation window so that it suits the stage A of the tensile test, for which only the FCC → HCP phase transformation is occurring. As can be seen in **Fig. 15**, this means that the slope of the curves macroscopic stress vs. lattice strains (in grey) during the tensile loading in stage A is similar to the slope of the curves temperature vs. lattice strains (in blue) obtained during cooling, except for the case of the {10.2} reflection, which exhibits a higher slope in stage A. For reminder the {00.2} basal slip is the only deformation mode in this stage. It comes along with a phase transformation which occurs in a plane shared by the two FCC and HCP crystallographic structures (i.e. the habit plane). From the beginning of stage B, a deviation from this linearity appears, leading to a lower evolution of the internal lattice strains with the macroscopic stress. The main deformation mode in stage B is twinning (mostly {10.2} type) which induces reorientations of the crystal lattice. Thus, a stress relaxation can be generated within twinned grains and causes a lattice strain decrease. In this stage a competition between twinning and phase transformation can therefore be highlighted. The comparison between the internal lattice strain values at the beginning of stage B shows that the {10.2} family plane deforms elastically less than the others before twinning. This result is consistent with the fact that, in the configuration (10.2) plane parallel to the sheet plane (c), the deformation can be accommodated by basal slip before that plasticity is controlled by twinning.

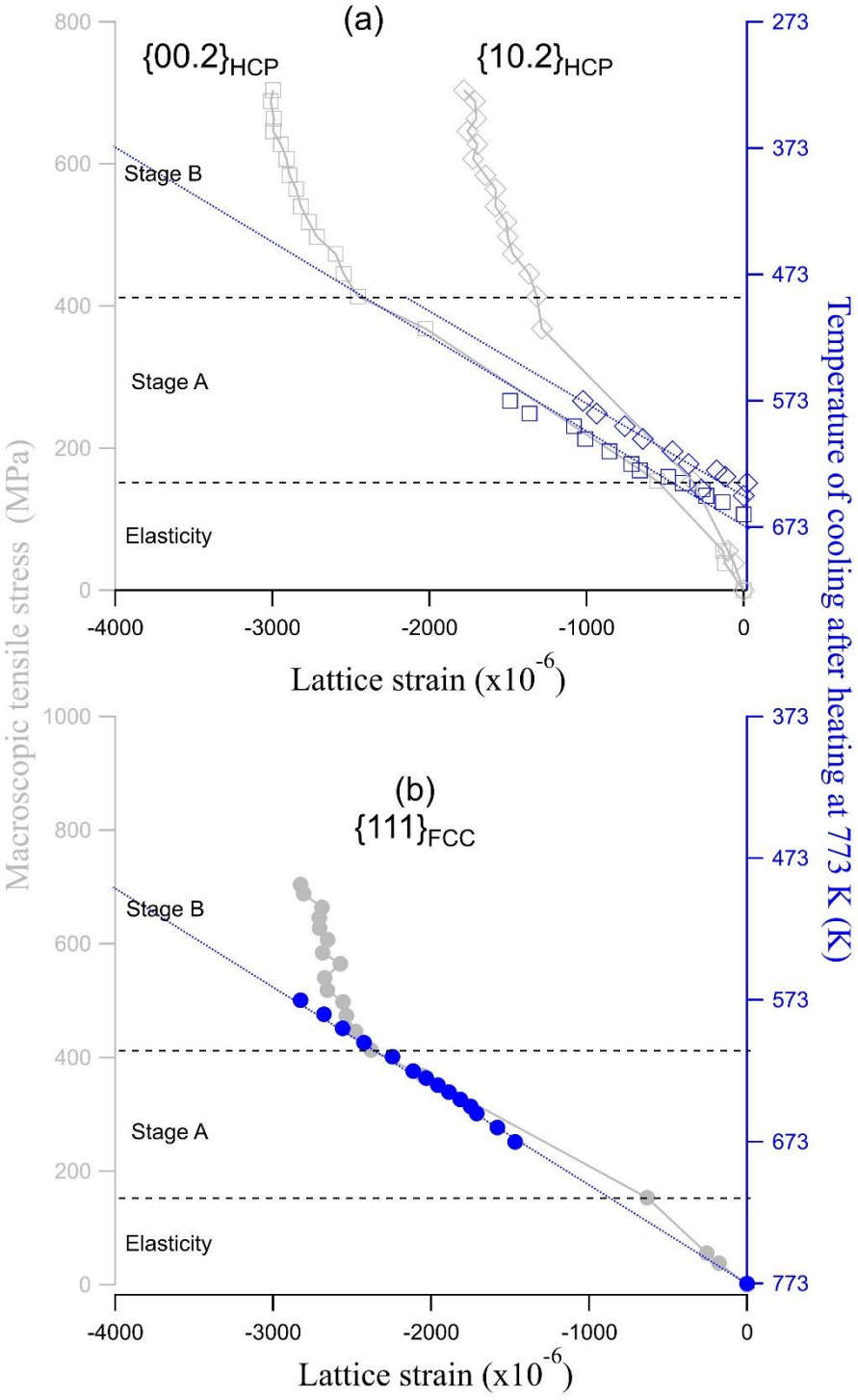

589

590 **Figure 15:** Example of lattice strains for $\{00.2\}_{HCP}$ and $\{10.2\}_{HCP}$ (a) and $\{111\}_{FCC}$ (b)
591 reflections during a tensile test along the rolling direction (grey symbol) with those
592 measured during a cooling stage after a heating at 773 K (blue symbol).

593

4. Conclusions

In the present work, new experimental results refresh and reinforce a scarce and dated to 1960's literature on phase transformations and strengthening mechanisms of polycrystalline cobalt. The specific *in situ* temperature experiments have showed that the FCC ↔ HCP phase transformation displays a temperature hysteresis between heating and cooling coupled to a macroscopic dilatometric hysteresis. However, the analysis of elastic lattice strains during the transformation does not exhibit this phenomenon. Complementary XRD studies of the phase transformation have highlighted the influence of the initial microstructure. In this work, a new and original *in situ* XRD study under mechanical loading has been performed revealing that the martensitic transformation of the initial FCC residual phase can be induced by the plasticity and coupled with the strain-hardening mechanisms. FCC to HCP transformation is activated by basal slip during the work-hardening stage A and continues during stage B with a competition with the twin mode.

References

[1] G. Bouquet, B. Dubois: Scr. Metall., 1978, vol. 12, pp. 1079–1081.
[2] A.E. Ray, S.R. Smith, J.D. Scofielf: J. Phase Equilibria, 1991, vol. 12, pp. 644–648.
[3] G. Fleurier, E. Hug, M. Martinez, P.-A. Dubos, C. Keller: Philos. Mag. Lett., 2015, vol. 95, pp. 122–130.
[4] H. Matsumoto: J. Alloys Compd., 1995, vol. 223, pp. L1–L3.
[5] H. Matsumoto: Phys. B Condens. Matter., 2003, vol. 334, pp. 112–117.
[6] C.R. Houska, B.L. Averbach, M. Cohen: Acta Metall., 1960, vol. 8, pp. 81–87.
[7] C.C. Sanderson: PhD Thesis, University of British Columbia, 1972.
[8] V.M. Marx, C. Kirchlechner, B. Breitbach, M.J. Cordill, D.M. Többens, T. Waitz, G. Dehm: Acta Mater., 2016, vol. 121, pp. 227–233.
[9] M. Martinez, G. Fleurier, F. Chmelík, M. Knapek, B. Viguier, E. Hug: Mater. Charact., 2017, vol. 134, pp. 76–83.
[10] A. Seeger, H. Kronmüller, S. Mader, H. Träuble: Philos. Mag., 1960, vol. 6, pp. 639–655.
[11] G. Fleurier, M. Martinez, P.A. Dubos, E. Hug: Mater. Sci. Forum., 2017, vol. 879, pp. 560–565.
[12] J.W. Christian, W. Hume-Rothery: Proc. R. Soc. Lond. Ser. Math. Phys. Sci., 1951, vol. 206, pp. 51–64.
[13] H.T. Hesemann, P. Müllner, E. Arzt: Scr. Mater., 2001, vol. 44, pp. 25–30.
[14] H.T. Hesemann, P. Müllner, O. Kraft, D. Nowak, S.P. Baker, K. Finkelstein, E. Arzt: Scr. Mater., 2003, vol. 48, pp. 1129–1133.
[15] H.-R. Wenk, S. Matthies, J. Donovan, D. Chateigner: J. Appl. Crystallogr., 1998, vol. 31, pp. 262–269.
[16] N. Bruzy: PhD Thesis, Ecole Centrale de Nantes, 2018.
[17] N. Bruzy, M. Coret, B. Huneau, G. Kermouche, M. Mondon, E. Bertrand, L. Stainier: Exp. Mech., 2019, vol. 59, pp. 1145–1157.
[18] W.A. Rachinger: J. Sci. Instrum., 1948, vol. 25, pp. 254–255.
[19] M.J. Buerger: Proc. Natl. Acad. Sci., 1940, vol. 26, pp. 637–642.
[20] J.T. Bonarski, M. Wróbel, K. Pawlik: Mater. Sci. Technol., 2000, vol. 16, pp. 657–662.
[21] W. Betteridge: Prog. Mater. Sci., 1980, vol. 24, pp. 51–142.
[22] K. Lonsdale, C. H. MacGillavry, G D. Rieck: International Tables for X-Ray Crystallography, Kynoch Press, 1962, vol 3.
[23] R. Bauer, E.A. Jaegle, W. Baumann, E.J. Mittemeijer: Philos. Mag., 2010, vol. 91, pp. 437–457.
[24] D. Gloaguen, B. Girault, B. Courant, P.-A. Dubos, M.-J. Moya, F. Edy, J. Rebelo Kornmeier: Metall. Mater. Trans. A., 2020, vol. 51, pp. 951–961.
[25] H. Bibring, F. Sebilleau: Rev. Métallurgie., 1955, vol. 52, pp. 569–578.
[26] G.W. Greenwood, R.H. Johnson: Proc. R. Soc. Lond. Ser. Math. Phys. Sci., 1965, vol. 283, pp. 403–422.
[27] G. Fleurier: PhD Thesis, Université de Caen, 2016.
[28] A. Zhou: PhD Thesis, Drexel University, 2008.
[29] A.G. Zhou, D. Brown, S. Vogel, O. Yeheskel, M.W. Barsoum: Mater. Sci. Eng. A., 2010, vol. 527, pp. 4664–4673.
[30] Y.N. Wang, J.C. Huang: Mater. Chem. Phys., 2003, vol. 81, pp. 11–26.

[31] J.W. Christian, S. Mahajan: Prog. Mater. Sci., 1995, vol. 39, pp. 1–157.
[32] M.H. Yoo: Metall. Trans. A., 1981, vol. 12, pp. 409–418.
[33] M. Martinez, E. Hug: Materialia, 2019, vol. 7, pp. 100420.
[34] S. Vaidya, S. Mahajan, C.M. Preece: Metall. Trans. A., 1980, vol. 11, pp. 1139–1150.
[35] Z. Nishiyama: Martensitic Transformation - 1st Edition, Academic Press, 1978.
[36] F. Sebilleau, H.Bibring: Inst. Met. Monogr., 1956, vol. 18, pp. 209–217.

Figures captions:

Graphical abstract: Evolution of metastable cobalt FCC volume proportion during thermal cycle and mechanical loadings.

Figure 1: EBSD Image Quality (IQ) map and phase cartography of as-received cobalt microstructure.

Figure 2: Diffraction patterns for $\{111\}_{FCC}$ and $\{00.2\}_{HCP}$ reflections during heating and cooling.

Figure 3: Volume fraction of FCC phase during heating (red circle) and cooling (blue square) of cobalt calculated from XRD data. Error bars are the standard deviation on the 8 couples of family planes.

Figure 4: Mechanical state during thermal cycle considering the different tracked plane families. (a) Lattice strain evolution during heating (red) and cooling (blue). (b) Thermal expansion coefficients during heating (red open circle) and cooling (blue open circle) obtained from XRD results. (c) Measured residual lattice strains after (black solid circle) the thermal cycle.

Figure 5: Dilatometric curves according to ε_{xx}, ε_{yy} and γ_{xy} during the thermal cycle. (x corresponds for this experiment to the rolling direction).

Figure 6: Influence of annealing conditions (temperature for a time of 1h (a) and time for a temperature of 1373°K (b)) on grain size and retained FCC phase proportion evolution.

Figure 7: Thermal loading paths in DSC performed for as-received (a), 573 K (b), 673 K (c) and 773 K (d) annealed samples with corresponding austenitic (red) and martensitic (blue) transformation peak tracking.

Figure 8: Temperatures of HCP → FCC and FCC → HCP transformations as a function of the number of applied DSC cycles (up to 30 cycles) of as-received sample superposed with the result of 573 K, 673 K and 773 K annealed samples.

Figure 9: FCC → HCP transformation evolution as macroscopic strain increases. Relationship between FCC phase proportion (red open triangle) and the deformation stages illustrated by work-hardening (black open square). Monitoring of the phase transformation anisotropy for various (φ, ψ) orientations (maps) during tensile straining with the corresponding average values (red solid circle).

Figure 10: $\{10.0\}_{HCP}$, $\{00.2\}_{HCP}$, $\{10.1\}_{HCP}$, $\{10.2\}_{HCP}$, $\{111\}_{FCC}$ and $\{200\}_{FCC}$ recalculated PFs of the as-received sample and of a sample strained at 7.8 % along RD.

Figure 11: Schematic representation of the orientation relationship between the FCC structure (in blue) and the HCP structure (in red) once shear has been achieved along the $[11\bar{2}]$ FCC direction.

Figure 12: Identification of {10.2}<10.1> tensile twinning system, {10.1}<10.2> compression twinning system and phase transformation on {00.2} and {10.0} PFs for the sample loaded up to 7.8 % strain (a). Schematic representation of reorientations caused by the two twin systems (b).

Figure 13: Identification of the phase transformation from $\{10.2\}_{HCP}$, $\{111\}_{FCC}$ and $\{200\}_{FCC}$ PFs for the sample loaded up to 7.8 % (a). Schematic representation of misorientations caused by the phase transformation (b).

Figure 14: Evolution of the integrated peak intensity at $\psi = 0°$ for the {10.2} reflection and around $\psi = 5°$ for the {00.2} reflection during a tensile test along the rolling direction.

Figure 15: Example of lattice strains for $\{00.2\}_{HCP}$ and $\{10.2\}_{HCP}$ (a) and $\{111\}_{FCC}$ (b) reflections during a tensile test along the rolling direction (grey symbol) with those measured during a cooling stage after a heating at 773 K (blue symbol).

Tables captions:

Table 1: XRD reflections tracked for each experiment and the plane family couples used for the phase volume fraction calculations.

Table 2: Applied temperatures for *in situ* XRD experiments during thermal cycle (heating rate 0.5 K/s between each temperature step – 1h acquisition duration for each temperature).

Table 3: {00.2} and {10.0} PF reorientations peculiar to twinning systems and phase transformation according to the 3 studied configurations.